Available online at www.sciencedirect.com
SCIENCE DIRECT®
International Journal of Heat and Fluid Flow 24 (2003) 372–388
International Journal of HEAT AND FLUID FLOW
www.elsevier.com/locate/ijhff

Large-eddy simulation of turbulent flow in a channel with rib roughness

Jie Cui *, Virendra C. Patel, Ching-Long Lin

IIHR—Hydroscience and Engineering and Department of Mechanical Engineering, The University of Iowa, Iowa City, IA 52242-1585, USA

Received 7 August 2002; accepted 9 January 2003

Abstract

Turbulent flow in a channel with transverse rib roughness on one wall is investigated by large-eddy simulation (LES). The spacing of the roughness elements is varied to reproduce the so-called d- and k-type roughness, and an intermediate roughness between the two. The time–mean and instantaneous flows are analyzed. The LES results agree with the rather limited laboratory observations in flows with rib roughness, and provide new insights into the effects of roughness on the mean flow as well as the turbulence structure. In d-type roughness, the outer flow almost rides over the roughness layer, in the mean, with the separation eddies confined to the gaps between the ribs. For intermediate roughness, between the d-type and k-type, the mean separation region is about the same size as the cavity between the ribs, but the outer flow is affected by large turbulent eddies emanating from the roughness layer. For k-type roughness, separation and reattachment occur between two adjoining ribs, much larger and more frequent eddies are thrown into the outer flow, resulting in strong interaction between the roughness layer and the outer flow. Time and space averaged velocity profiles show the well-known downward shift of the semi-logarithmic portion of the law of the wall. This result is quite surprising in view of the grossly varying spatial structure of the instantaneous flow.

Keywords: Channel flow; Turbulence; LES; Surface roughness

1. Introduction

Turbulent flow over a rough surface is an important problem in fluids engineering and has been the subject of numerous studies in diverse fields, such as aerodynamics, hydrodynamics, hydraulics, fluids machinery, and atmospheric flows. The flow over a surface fitted with transverse, rectangular ribs of varying height, width and spacing is often used as a simple model to study roughness effects on friction factor and heat and mass transfer.

Early experimental studies led to correlations between the roughness height and the roughness function, namely, the downward shift in the semi-logarithmic portion of the law of the wall. These results are now found in textbooks along with similar correlations for other types of roughness (see, for example, White, 1991).

Perry et al. (1969) studied the turbulent boundary layer over a wall roughened by transverse ribs, and proposed to divide the roughness into two types: k-type and d-type. The letter denotes the significant length scale that determines the roughness function, velocity profiles and friction factor, k being the roughness height and d the boundary-layer thickness, pipe diameter, or channel height. Tani (1987) suggested that, for regularly spaced ribs, a demarcation between k-type and d-type roughness might be made at the pitch ratio $w/k = 4$, where w is the pitch between the roughness elements. For d-type roughness, typified by closely spaced ribs with w/k less than 4, the roughness function (downward shift in the semi-logarithmic law) is independent of the size of roughness. In this case, the ribs are so closely spaced that stable vortices are set up in the grooves, eddy shedding from the roughness elements into the outer flow is negligible, and the outer flow is relatively undisturbed by the roughness elements (making it independent of k). For k-type roughness, typified by a wall roughened by sparsely spaced transverse ribs or rods, with w/k greater than 4, eddies with length scale of the

* Corresponding author. Present address: Mechanical Engineering Department, Tennessee Technological University, P.O. Box 5014, Cookeville, TN 38505, USA. Tel.: +931-372-3357; fax: +931-372-6340.
E-mail address: jiecui@tntech.edu (J. Cui).

0142-727X/03/$ - see front matter © 2003 Elsevier Science Inc. All rights reserved.
doi:10.1016/S0142-727X(03)00002-X

order of the roughness height are shed from the roughness elements and penetrate into the bulk flow toward the pipe or channel center (or boundary layer edge), and the roughness function and the friction factor depend on the size of the roughness elements.

Most early researchers studied just one or a limited number of rib roughness configurations, and data were typically taken at only one location within the rib cycle (Antonia and Luxton, 1971; Islam and Logan, 1976; Siuru and Logan, 1977). More attention has been given to turbulence intensities, Reynolds shear stresses, and flow variations along the ribbed surface in some recent investigations. For example, Hanjalic and Launder (1972) carried out detailed experimental examination of fully developed asymmetric flow in a plane channel. One of the surfaces was roughened by square-sectioned silver steel ribs with a pitch-to-height ratio of 10, while the other was left smooth. The mean velocity distribution between the surfaces exhibited three distinct regimes. Near the smooth wall, the profile was in good accord with the "law of the wall". Near the rough wall, the downward shift from the "law of the wall" was identified, while in the central region of the channel, the mean flow displayed strong interaction between the two wall regions. Liou et al. (1990, 1993b) presented laser Doppler velocimetry (LDV) measurements of mean velocity, turbulence intensity, and Reynolds stresses in fully developed flow in a channel with square ribs distributed on both walls. A pitch ratio of 10 was found to be optimal from the standpoint of heat transfer enhancement. The reattachment length behind the rib was found to be a function of the pitch ratio. Large turbulence kinetic energy and significant anisotropy occurred in the shear layers and separated-flow regions. The peak of the turbulence kinetic energy was found to occur at approximately one rib-height upstream of reattachment, and the minimum occurred inside the separated recirculating zone and near the corner, with a value only about one-fifth of the aforementioned peak value.

Okamoto et al. (1993) measured the flow structure over repeated two-dimensional square ribs mounted on a plane surface in a water channel. Mean velocity, static pressure, velocity vector, turbulence intensity, and integral scale were obtained. The turbulence intensity and heat transfer were maximized and the flow reattached within the groove with a pitch ratio of 9. They found that the effects of Reynolds number on the optimum pitch ratio for augmenting turbulence seemed to be insignificant. They also reported that at the optimum pitch ratio, the pressure loss due to the ribs was maximized. This was the cost of augmentation of heat transfer. Okamoto et al. also made flow visualizations that confirmed the demarcation between d- and k-type roughness suggested earlier by Tani.

Most recently, Djenidi et al. (1999) carried out LDV measurements and flow visualizations in a turbulent boundary layer over d-type roughness with a pitch ratio $w/k = 1$. The near-wall quasi-streamwise vortices and low-speed streaks were found to be similar to those in a smooth-wall turbulent boundary layer. They claimed the outflows from the cavities into the outer flow were responsible for the local maximum in the Reynolds shear stress over the cavities. The form drag over rough surfaces was observed to be dominant compared with the friction drag.

There are several numerical studies related to flow over rough surfaces. As indicated in the recent review by Patel (1998), most solve the Reynolds-averaged Navier–Stokes (RANS) equations with relatively simple turbulence models and do not explicitly calculate the flow in the roughness layer. Instead, they rely on the law of the wall with a specified roughness function. For channel flow with ribs such calculations were made by Durst et al. (1988), Liou et al. (1993a), and Bredberg and Davidson (1999). In general, the computed mean velocities matched well with experimental results, but significant differences were found between the calculated and measured turbulence kinetic energy in the separated-flow and near-wall regions, which the authors attributed to the use of the law of the wall in the boundary conditions and deficiencies of the turbulence models. Large-eddy simulation (LES) of flow and heat transfer in a rib-roughened channel was carried out by Ciofalo and Collins (1992). The Smagorinsky model with van Driest damping near the walls was implemented to model sub-grid scale effects. Since the focus was on the demonstration of the feasibility of LES for simple and complex flows rather than accuracy, a rather coarse grid ($48 \times 24 \times 24$) was selected. The rib height was 1/4.8 of the channel height and the pitch-to-height ratio was 7.2. The mean flow rate and the turbulence levels in the bulk flow region were over-predicted by LES as compared with experimental data and k–ε simulations. However, the authors claimed that the overall flow structure and many fine features of the mean and fluctuating flow fields were in qualitative agreement with experimental data. Miyake et al. (2001) performed direct numerical simulation of rough-wall heat transfer in turbulent flow in a channel. Sand grain roughness and regularly arranged two-dimensional ribs (k-type) were considered. It was shown that the total drag on a rough wall was composed of much larger pressure drag than friction drag. The major effect of the roughness element was to enhance the turbulent mixing and heat exchange. The mixing was controlled by large scale motions, which were inherent to the logarithmic layer.

In the present work we employ LES with a dynamic sub-grid-scale model (DSM) to simulate turbulent flow in a channel with one wall roughened by square ribs. The principal objectives of the study are to investigate the flows that lead to the so-called d-type and k-type roughness effects, the turbulence structure associated

with these flows, the interaction between the roughness layer and the outer flow, and most important, to determine the relation between the flow in the roughness layer and the roughness function associated with the time- and space-averaged velocity profile.

Following the results of the flow visualizations of Okamoto et al. (1993), three different pitch ratios: $w/k = 1$, 4, and 9, are selected in an attempt to reproduce d-type, intermediate, and k-type roughness. The following section briefly describes the numerical method and the geometrical configuration. Section 3 describes the time-averaged quantities of the simulation results and comparisons with published laboratory measurements. In Section 4, the results are analyzed in the classical framework of treating ribs as surface roughness. The instantaneous flow fields are presented in Section 5. Section 6 provides a summary of major results and conclusions.

2. Numerical method and flow geometry

The three-dimensional, unsteady, incompressible, filtered continuity and Navier–Stokes equations, (1) and (2), respectively, are solved with a DSM:

$$\frac{\partial \bar{u}_i}{\partial x_i} = 0 \tag{1}$$

$$\frac{\partial \bar{u}_i}{\partial t} + \frac{\partial}{\partial x_j}(\bar{u}_i \bar{u}_j) = -\frac{1}{\rho}\frac{\partial \bar{p}}{\partial x_i} + \nu\left(\frac{\partial^2 \bar{u}_i}{\partial x_j \partial x_j}\right) - \frac{\partial \tau_{ij}}{\partial x_j} - \frac{1}{\rho}\frac{\partial P}{\partial x}\delta_{1i} \tag{2}$$

Here $i = 1$, 2, and 3, $\bar{u}_i$ are the resolved velocity components (corresponding to $\bar{u}$, $\bar{v}$, and $\bar{w}$, respectively, $\bar{u}_i = u_i - u'$, where u' are sub-grid-scale (SGS) components), x_i are the Cartesian coordinates (corresponding to x, y, and z, respectively), $\bar{p}$ is pressure, ν is kinematic viscosity, $\partial P/\partial x$ is the mean pressure gradient imposed in the streamwise direction to drive the flow, δ_{1i} takes value of one only when $i = 1$, and

$$\tau_{ij} = \overline{u_i u_j} - \bar{u}_i \bar{u}_j \tag{3}$$

is the sub-grid-scale stress representing the effect of small-scale motions.

In DSM, the model coefficients are computed dynamically as the calculation progresses rather than being prescribed a priori. Two filters are introduced and applied in all three coordinate directions: the grid filter and the test filter. A test filter twice as large as the grid filter is usually chosen and is used in this paper. By applying the test filter to the equations, the sub-grid-scale stresses on the test level, or sub-test-scale stresses can be constructed. Then the sub-grid-scale stresses are parameterized by an eddy-viscosity model

$$\tau_{ij} - \frac{\delta_{ij}}{3}\tau_{kk} = -2C\overline{\Delta}^2 |\overline{S}| \overline{S}_{ij} \tag{4}$$

where

$$|\overline{S}| = (2\overline{S}_{ij}\overline{S}_{ij})^{1/2}, \quad \overline{S}_{ij} = \frac{1}{2}\left(\frac{\partial \bar{u}_i}{\partial x_j} + \frac{\partial \bar{u}_j}{\partial x_i}\right),$$

δ_{ij} is the Kronecker delta, $\overline{\Delta} = (\Delta x_1 \Delta x_2 \Delta x_3)^{1/3}$, Δx_i are the mesh distances, and C is a model constant. To obtain a single coefficient from these independent equations, C is assumed to remain unchanged between the two filters (Germano et al., 1991; Piomelli, 1993; Lilly, 1992). Then, the model constant C can be determined from

$$C = \frac{1}{2}\frac{L_{ij}M_{ij}}{M_{ij}M_{ij}} \tag{5}$$

where $L_{ij} = \overline{\overline{\bar{u}_i \bar{u}_j}} - \overline{\bar{u}_i}\,\overline{\bar{u}_j}$ and $M_{ij} = \overline{\Delta}^2 \overline{|\overline{S}|\overline{S}_{ij}} - \overline{\overline{\Delta}}^2 \overline{|\overline{S}|}\,\overline{\overline{S}_{ij}}$ (double over-bar represents test-scale resolved quantities) can be directly computed from the resolved motion. In the present simulation, C is averaged in the spanwise direction and a cutoff is set to make the total viscosity non-negative to prevent any instability caused by negative viscosity. Since C is averaged in the spanwise direction, the cutoff is applied for very few points for a typical time step.

The finite-volume LES numerical code used here was developed by Zang et al. (1994). In this method, the governing equations in general curvilinear coordinates are discretized on a non-staggered grid. A fractional-step method is employed and the pressure Poisson equation derived from the equation of continuity is solved with multigrid acceleration. Time marching is semi-implicit with formal accuracy of second order in both space and time. Zang et al. (1994) verified and validated the code in various flows, including decaying vortices, lid-driven flow in two-dimensional, three-dimensional and polar cavities, flow over a backward-facing step, and flow in a curved square duct.

In all the simulations presented in this paper, a mean pressure gradient is imposed in the streamwise direction to drive the flow. The imposed pressure gradient is carefully adjusted to keep the Reynolds number (Re), based on the bulk velocity (U_b) and half-channel height ($H/2$), constant at 10,000 for all the cases. The viscosity ν is taken as $5 \times 10^{-5} U_b H$. Periodic boundary conditions are imposed in both the streamwise (x) and spanwise (y) directions. No-slip boundary conditions are applied at the top and bottom channel boundaries. The numerical method is first applied to a smooth plane channel flow. The computational domain is $2H$ in length, and H in height and width. The mean velocity profile in the semi-logarithmic format obtained from a $162 \times 42 \times 130$ grid (in streamwise, spanwise and wall-normal directions, respectively) is plotted in Fig. 1. The first grid point near the wall is located at $z^+ = 1$, and

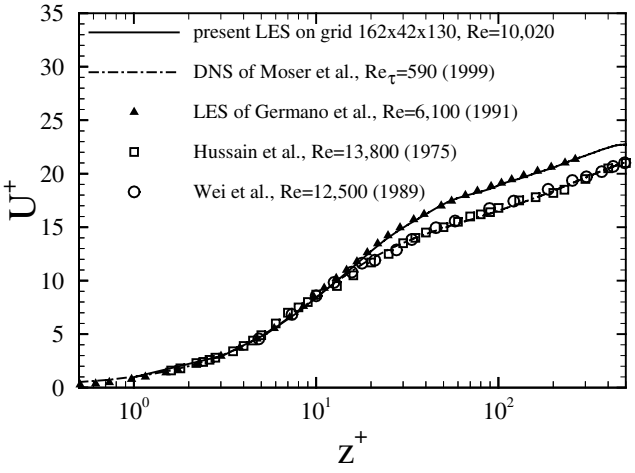

Fig. 1. Mean velocity profile in wall coordinates for plane channel flow.

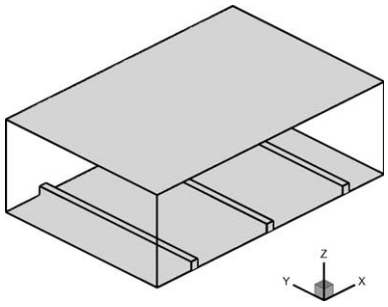

Fig. 2. Three-dimensional geometry of channel flow with repeated ribs (k-type).

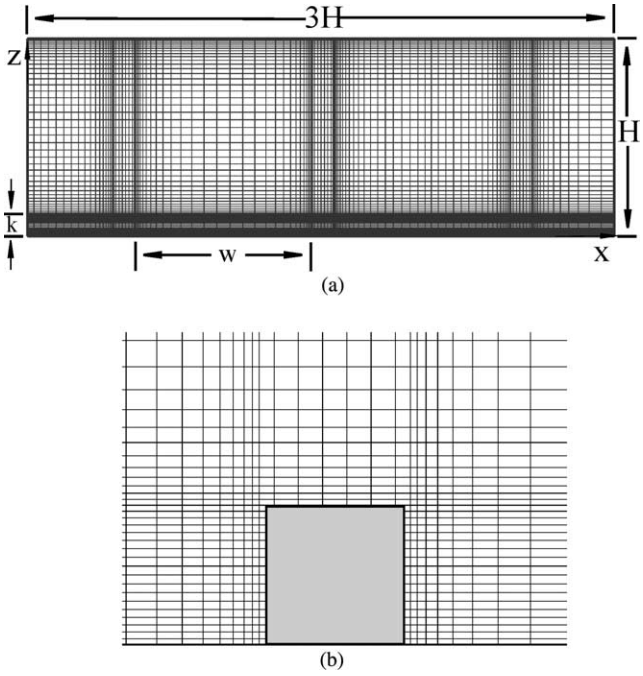

Fig. 3. (a) Computational grid for channel flow with repeated ribs (k-type); (b) refined mesh around rib.

then stretched out in the wall-normal direction, while in streamwise and spanwise directions, the grid is uniformly distributed. The present LES profile matches well with the results of LES by Germano et al. (1991) who employed a pseudo-spectral method to solve the channel flow at $Re = 6100$ on a $48 \times 56 \times 64$ grid. However, compared with the experiments of Hussain and Reynolds (1975), Wei and Willmarth (1989), and DNS of Moser et al. (1999), both LES calculations slightly over predict the velocity in the logarithmic region. The deviation (both over-prediction and under-prediction) of the LES profile from the log-law was also reported by Najjar and Tafti (1996) in a study of discrete test filters and finite difference approximations for the DSM. The effects of discrete test filters applied in physical space on the dynamic constant and the interaction of the dynamic procedure with finite difference approximations to the governing equations were investigated. They found that the inclusion of the dynamic model would not always result in better predictions of the flow field. At the same time, the model and numerics were intimately intertwined and it maybe difficult and impractical to isolate one from the other. This discrepancy was not pursued further in the current study.

Fig. 2 shows the channel geometry with repeated ribs. A Cartesian grid, shown in Fig. 3, is used with a finer spacing close to the channel walls and ribs to resolve the near-wall flow. Two-dimensional ribs of same height and width are uniformly distributed on the lower wall. The rib height k is 10% of the channel height H. For d-type roughness, 10 ribs are distributed on the lower wall, making the pitch ratio $w/k = 1$. The computational domain remains $2H \times H \times H$ (length $\times$ height $\times$ width). Simulations are performed on two grids: $162 \times 42 \times 66$ and $162 \times 42 \times 130$. The results from the two meshes are quite close, so the grid spacing from the $162 \times 42 \times 66$ mesh (first grid point is $0.002H$ away from the rib surfaces in all directions) is employed for all three types of roughness. Depending on the local friction velocity, it falls into a range of 0.2–2 in terms of wall units. There are 20 cells from the bottom of the channel to the top of the rib and 46 cells from the rib top to the channel top. In the spanwise direction, uniform grid is used with a resolution of 27 wall units based on the friction velocity on the top smooth surface.

For intermediate and k-type roughness, it was found from two-point correlations that the simulation domain of $3H \times 2H \times H$ must be used to resolve large-scale energy containing eddies. With this domain size, intermediate roughness is represented by six ribs with a pitch ratio of 4, while k-type roughness is represented by three ribs with a pitch ratio of 9. A grid size of $122 \times 82 \times 66$, which yields the optimal grid spacing determined previously, is used for these two simulations.

3. The mean flow

3.1. Mean velocity profiles and streamlines

Time and spanwise averaged velocity profiles are displayed in Fig. 4. The time-averaging is performed on 5000 samples over a period of about 3 large-eddy turnover time (H/u_τ, where u_τ is the friction velocity on the top wall) after the flow reaches a "quasi-steady" state. For d-type roughness, the velocity profiles appear similar regardless of streamwise location. They resemble the velocity profile in a flat channel with a reduced height of $H - k$. The roughness layer has little impact on the core flow except that the ribs block the mass flow within the roughness layer, displacing the flow up by a distance of the rib height. The velocity magnitude in the cavities between the ribs is small.

Intermediate roughness disturbs the mean flow to a greater extent. Velocity profiles at various locations differ significantly. The flow responds to expansion and contraction of the flow passage with deceleration and acceleration. Separation zones behind the ribs are longer than for d-type roughness where they are necessarily of length W. The location of maximum velocity shifts toward the upper wall.

For k-type roughness, the velocity distributions depend on the streamwise location. Separation, reattachment, and further detachment occur in the grooves between the ribs. The ribs alter the flow in the entire channel and the maximum velocity occurs much closer to the top wall. The results clearly show the effectiveness of k-type roughness in augmenting the momentum (and heat and mass) exchange between the roughness layer and the outer flow.

Streamlines for the three types of rib roughness are displayed in Fig. 5. For d-type roughness, the portion from $x/H = 0.8$ to 1.2, including the 5th and 6th ribs, is shown. Streamlines beyond the rib height are nearly parallel. A vortex fills the cavity between the two ribs. For intermediate roughness, a vortex of the same size as the groove is formed between the ribs. This vortex prevents the outer flow from reattaching to the channel floor within the groove. A smaller vortex with opposite

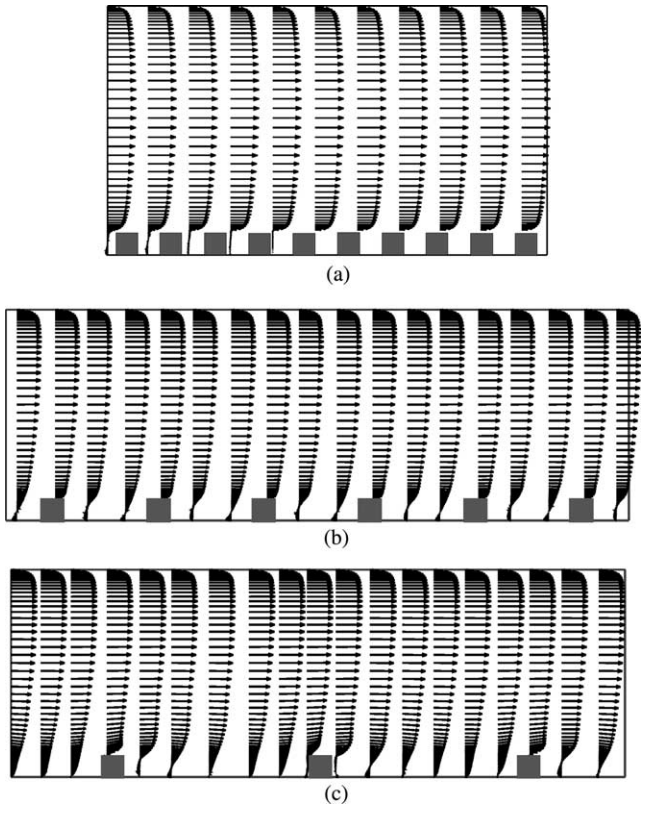

Fig. 4. Mean velocity vectors at different locations in the channel: (a) d-type roughness; (b) intermediate; (c) k-type roughness.

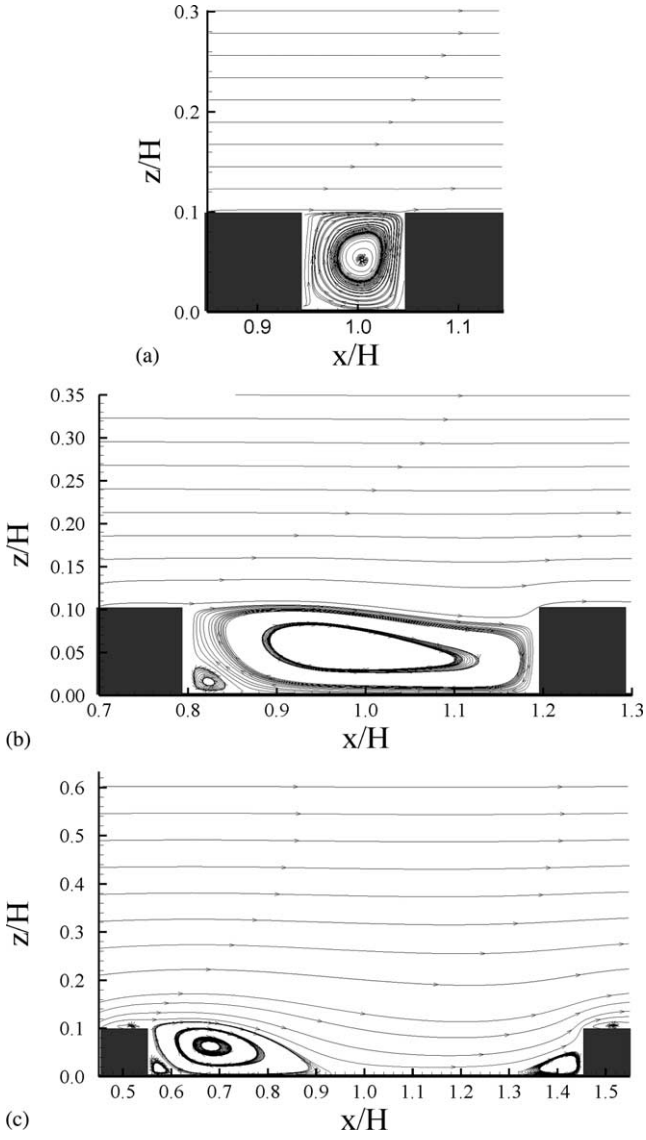

Fig. 5. Mean streamlines for (a) d-type roughness, (b) intermediate roughness, and (c) k-type roughness.

circulation is found in the lower corner behind the rib. Streamlines above the cavity are still nearly parallel except near the rib. Streamlines for k-type roughness reveal four separation zones associated with the ribs. A small separation zone is formed on the rib top as the sharp front edge of the rib deflects the flow from the previous groove. A large separation region is downstream of the rib, accompanied by a small vortex at the lower corner behind the rib. Flow reattaches to the channel floor within the groove and detaches again, forming a vortex upstream of the next rib. Interestingly, the reattachment point is about four times the rib height, the rib spacing in the intermediate roughness case. Though streamlines far away from the ribs are nearly parallel, in the lower half of the channel they undulate in response to rib geometry. A free shear layer is located above the separation region and downstream of the rib.

3.2. Comparisons with experimental measurements

Mean streamwise velocity profiles on the rib top and in the middle of the cavity between the ribs are compared with measurements of Okamoto et al. (1993) and by Djenidi et al. (1999) in boundary layers. The measurements were made at points beyond the roughness height. They are normalized by the free stream velocity and boundary layer thickness. For meaningful comparisons, the present channel flow results are normalized by the maximum streamwise velocity and distance to the maximum velocity. The Reynolds numbers in the measurements are recalculated on the basis of characteristic velocity (bulk velocity) and length scale (five times the rib height, which is the half channel height) used in the present LES simulations.

For d-type roughness, measurements of Djenidi et al. (1999) are available only at the cavity center. Measurements by Okamoto et al. (1993) are available at both at cavity center and the rib top. In the cavity, the velocity starts with a negative value, indicating reversed flow. It reaches minimum at $z/H = 0.02$, then increases almost linearly to rib height (Fig. 6). Flow within the cavity is similar to the two-dimensional lid-driven cavity flow at low Reynolds number, since the velocity magnitude inside the cavity is quite small. Outside the cavity, the velocity grows quickly in a short distance through a thin shear layer. Present LES results match well with the measurements of Djenidi et al. (1999). Both differ from measurements of Okamoto et al. (1993). Streamwise velocity approaches its maximum at $z/H = 0.62$. A comparison of the velocity profiles at the rib center (Fig. 6(a)) and in the cavity (Fig. 6(b)) from either Okamoto et al. (1993) or the present results indicates they are almost the same. The ribs generate disturbances in the main flow more like a single object on the channel floor rather than as individual ribs. The rib effect on velocity

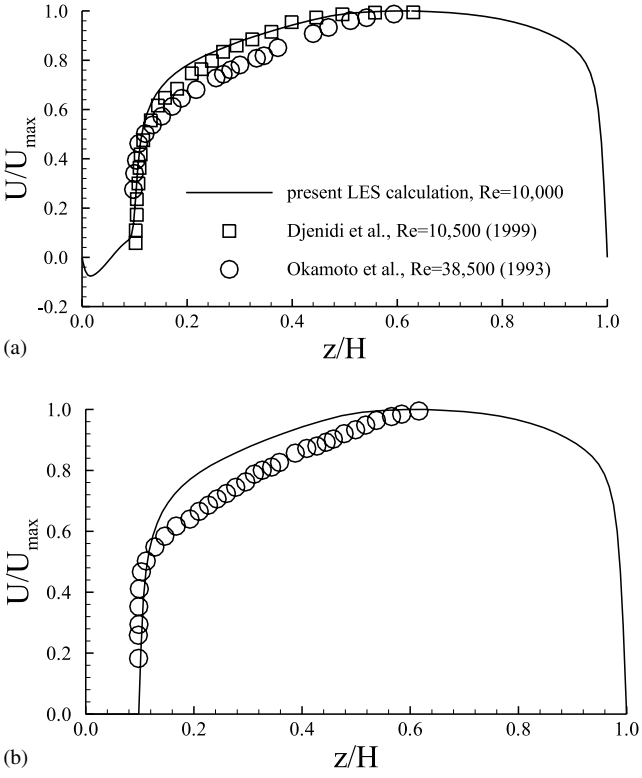

Fig. 6. Comparisons of mean streamwise velocity profiles with experimental data at cavity and rib for d-type roughness: (a) at cavity; (b) at rib.

is seen in the slightly asymmetric profile with a maximum at $z/H = 0.62$. The primary effect is that mass flow is blocked by the ribs.

Fig. 7 compares streamwise velocity with measurements of Okamoto et al. (1993) with intermediate roughness, with $w/k = 4$. In the cavity, the magnitude of negative velocity is larger than in d-type roughness, implying stronger reversed flow. After a negative minimum very close to the bottom wall the velocity increases gradually to a maximum at $z/H = 0.8$. The ribs push the location of the maximum velocity much closer to the top wall than in d-type roughness. At the rib center, the velocity profile differs significantly from that in the cavity. Flow becomes more sensitive to streamwise location. Present LES is in good agreement with the measurements, suggesting that the Reynolds number effects are less pronounced than for d-type roughness. This is also found from experimental studies, and is to be expected from the fact that with d-type roughness the flow resembles that in a smooth channel and there is a comparatively larger surface area for viscous effects to act on.

Velocity profiles for k-type roughness are presented in Fig. 8. At the cavity center, the flow has just reattached to the bottom, so there is no negative velocity at the midpoint. At the rib center, a small portion of reversed flow is found due to detached flow from the

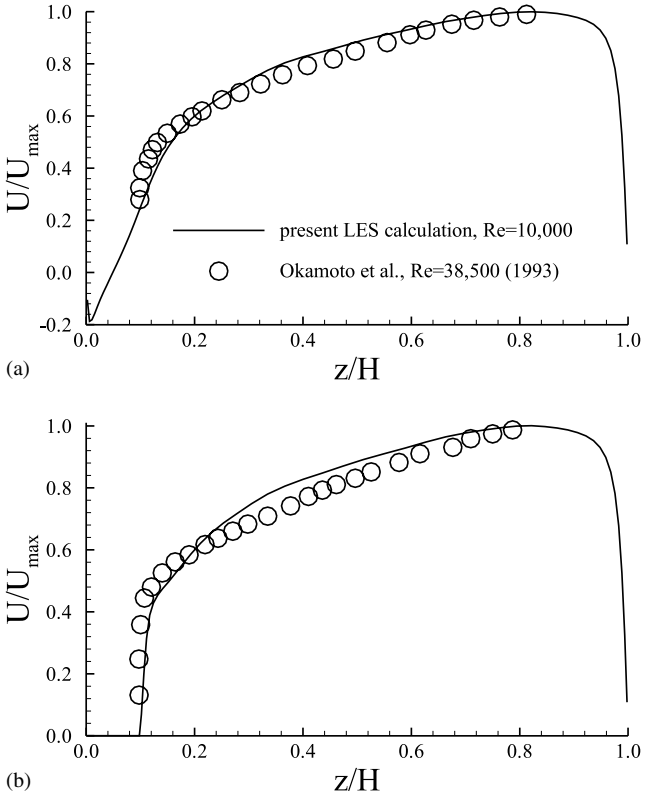

Fig. 7. Comparisons of mean streamwise velocity profiles with experimental data at cavity and rib for intermediate roughness: (a) at cavity; (b) at rib.

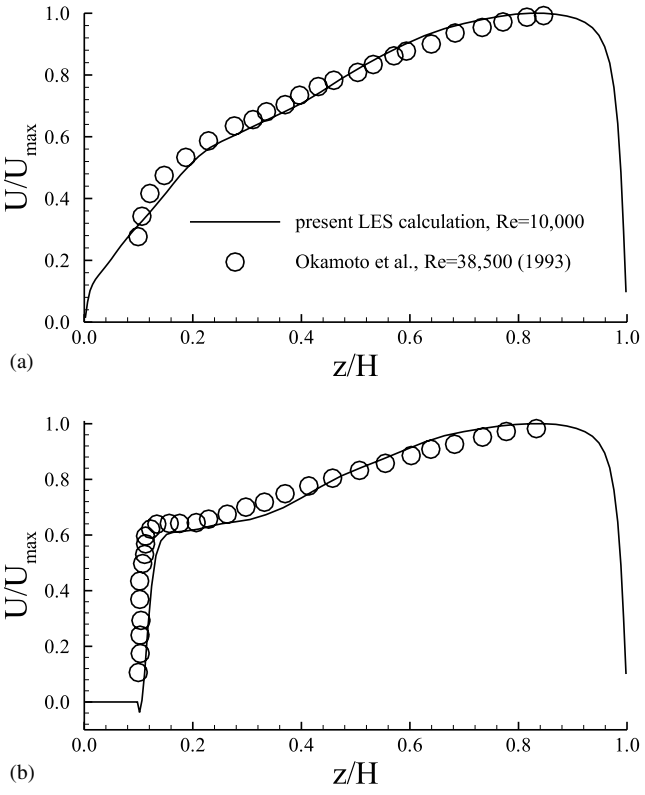

Fig. 8. Comparisons of mean streamwise velocity profiles with experimental data at cavity and rib for k-type roughness: (a) at cavity; (b) at rib.

previous cavity. Flow accelerates over the rib due to contraction of the cross-section. A velocity overshoot is formed above the rib. The calculations agree well with the measurements, again implying little Reynolds number effects for k-type roughness.

3.3. Regions affected by surface roughness

Though the flow field changes dramatically on the lower wall due to the ribs, the mean velocity profiles are not significantly affected beyond some distance from the bottom wall. Fig. 9 shows velocity profiles at four streamwise locations; the distance x is measured from the back face of the upstream rib and $x/w = 0.5$ is at the center of the cavity between the ribs. For d-type roughness, all velocity profiles collapse on each other right above the rib top. For intermediate roughness, velocity profiles become indistinguishable beyond z/H of about 0.2. For k-type roughness, this region extends to about z/H of 0.4. These observations suggest that the flow over rough surfaces may be divided into two distinct regions: an inner region where the flow strongly depends on the roughness geometry, and an outer one where it is essentially independent of the wall geometry. The beginning of the outer region is strongly related to the roughness geometry and Reynolds number.

Fig. 9 also sheds some light on limits of conventional modeling of flow over rough walls. In the so-called wall functions approach to using turbulence models in Reynolds averaged Navier–Stokes equations, the near-wall flow is not resolved and boundary conditions for velocity and turbulence parameters are imposed in this outer layer where the flow has lost memory of the spatial structure of the roughness. Clearly, the present LES results suggest that such an approach is justified only if it is applied at quite large distances in the case of k-type roughness. This point is discussed further in a later section.

3.4. Wall shear stress and pressure

Fig. 10 shows the wall shear stress distributions between successive ribs. The friction coefficient, C_f, is defined as

$$C_f = \frac{\tau_w}{\frac{1}{2}\rho U_b^2} \tag{6}$$

where the wall shear stress τ_w is calculated in the usual way, from the slope of the velocity profile at the wall. The x-axis starts from the back face of the upstream rib. It extends upstream along the back face, the top and the front face, and goes downstream until the front of the

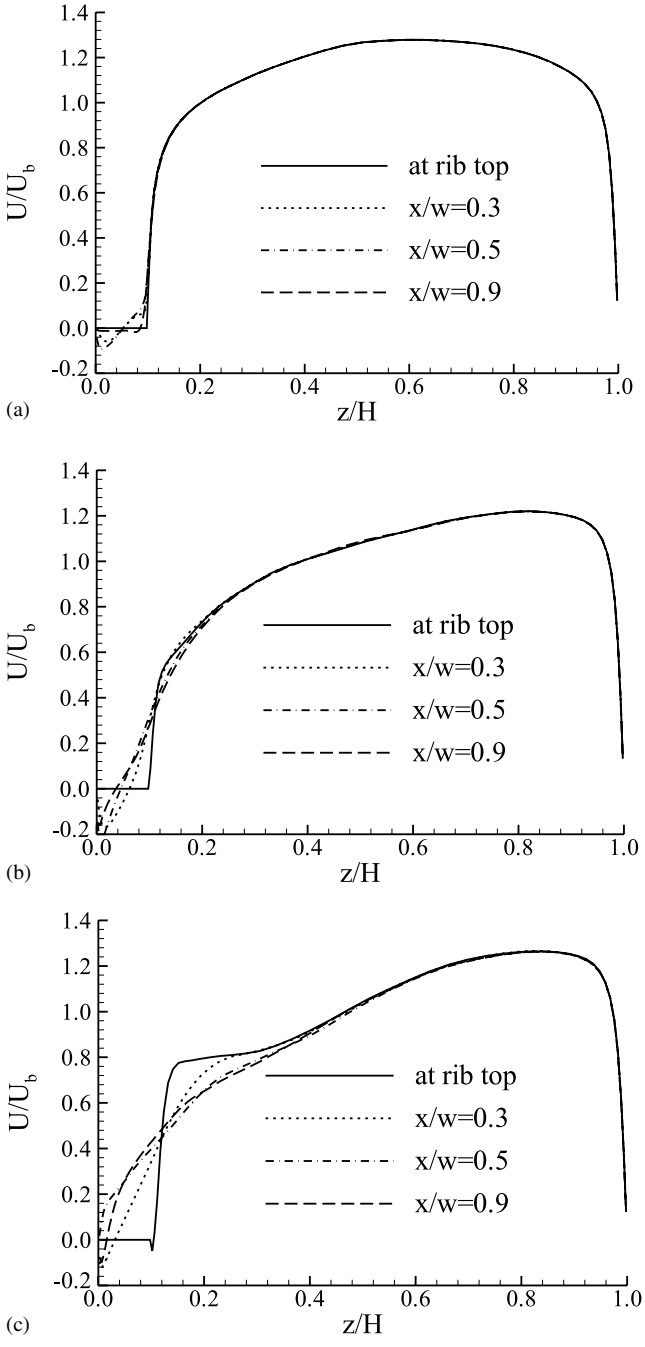

Fig. 9. Mean streamwise velocity profiles at different locations for (a) d-type roughness, (b) intermediate roughness, and (c) k-type roughness.

downstream rib. The distance is normalized by the rib height k.

For d-type roughness, where the cavity is filled with separated flow, C_f is negative on the entire cavity floor. The reversed flow is very weak, and the magnitude of C_f is quite small compared to intermediate and k-type roughness. On the rib top, d-type roughness shows positive C_f values, highest among the three roughness types. For intermediate roughness, C_f has a small positive value up to $x/k = 0.6$ due to the small vortex in the lower corner behind the rib rotating in opposite sense to the main vortex (Fig. 5(b)) and becomes negative, with a minimum at $x/k = 2.3$, over the rest of the cavity. For k-type roughness, C_f changes sign several times. It begins with a small positive value in the small separation zone at the lower corner behind the rib (Fig. 5(c)), turns negative at $x/k = 0.6$ with a minimum at $x/k = 2.3$, and then positive at $x/k = 4.3$ as the flow reattaches to the floor, and finally negative again at $x/k = 7.0$, due to separation in front of the downstream rib. On the rib top, C_f takes negative values indicating flow separation.

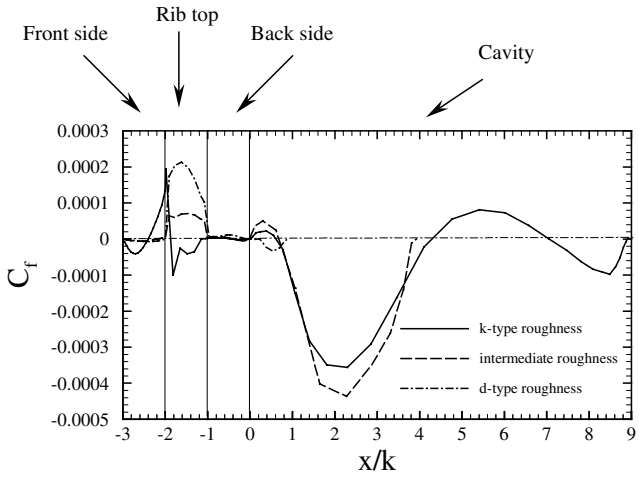

Fig. 10. Wall shear stress distribution between consecutive ribs.

Fig. 11 displays the pressure distribution (including the mean pressure gradient $\partial P/\partial x$) on the groove floor. The pressure coefficient, C_p, is defined as

$$C_p = \frac{p - p_{ref}}{\frac{1}{2}\rho U_b^2} \tag{7}$$

The pressure at the rear corner of the upstream rib is chosen as the reference pressure. For d-type roughness, the pressure is almost uniform and quite small in the cavity. For intermediate and k-type roughness, the flow experiences strong acceleration and favorable pressure

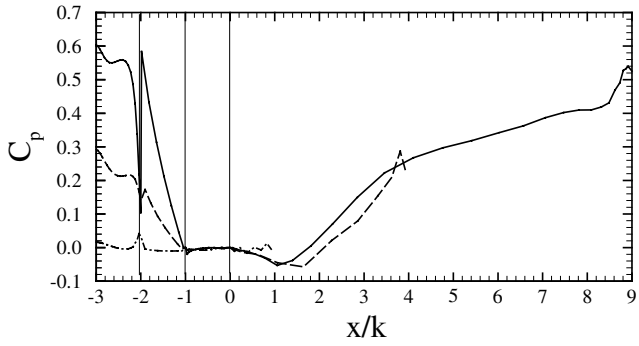

Fig. 11. Wall pressure distribution between consecutive ribs.

gradient on the rib top. This trend remains until $x/k = 1.2$ in spite of the cross-sectional area expansion downstream of the rib. The pressure gradually becomes adverse in the rest of the cavity. The pressure coefficient on the front face of the rib is quite high for k-type and intermediate roughness because of flow impingement. On the back face of the rib, a recirculation region is formed and both C_p and C_f are essentially zero for all three types of roughness.

3.5. Turbulence intensities

Turbulence (rms) intensities in the streamwise and wall-normal directions at the center of the cavity in d-type roughness are shown in Fig. 12 along with experimental data. U_{rms} and W_{rms} are defined as $\sqrt{\langle(\bar{u} - \langle\bar{u}\rangle)^2\rangle}/U_b$ and $\sqrt{\langle(\bar{w} - \langle\bar{w}\rangle)^2\rangle}/U_b$, respectively, where $\langle\cdot\rangle$ stands for time and spanwise average. The calculated U_{rms} is small inside the cavity with a peak located close to the floor. It increases rapidly to a maximum of 0.15 and decreases gradually to a minimum at $z/H = 0.68$. As expected, U_{rms} reaches a second peak close to the top wall of the channel before decreasing toward the wall. The two peaks have about the same value, as in a flat channel. The minimum between the two peaks, however, shifts upward due to the effect of the ribs. The calculated peak value above the rib matches well the experiment of Djenidi et al. (1999). The measured U_{rms} drops more quickly and to a lower value than in the present calculation. The difference is due by the fact that the experimental measurements were made in boundary layer flow, where the turbulence intensities vanish outside the boundary layer. The Reynolds number effect causes the measurements of Okamoto et al. (1993) to differ from both the current LES results and the measurements of Djenidi et al. (1999).

The peak value of turbulence in the vertical direction, W_{rms}, for d-type roughness (Fig. 12(b)) is much smaller than that of U_{rms}. Like the streamwise component, W_{rms} grows quickly from a small value within the cavity to a maximum just above the rib height. It has another peak close to the top wall. Between the peaks, the minimum is at $z/H = 0.64$. In contrast to U_{rms}, the peak value of W_{rms} above the rib height is higher than that close to the top wall, indicating a larger effect of the ribs on the vertical fluctuations than on the streamwise component.

For intermediate roughness, the peak values of U_{rms} at the groove and rib are higher than those near the top wall (Fig. 13). The peak value over the rib is slightly higher than that at the cavity. The calculated U_{rms} matches the experimental data well in the area above the rib height. In the upper half of the channel, the measurements drop more quickly than in the present simulations because the experimental data is from a

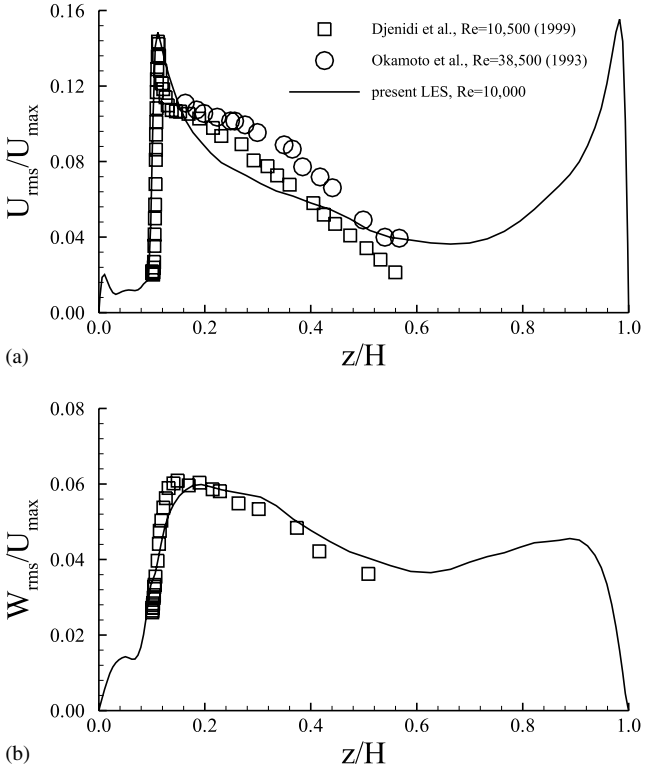

Fig. 12. Comparisons of mean streamwise and vertical turbulence intensities with experimental data at cavity for d-type roughness: (a) streamwise component U_{rms}; (b) vertical component W_{rms}.

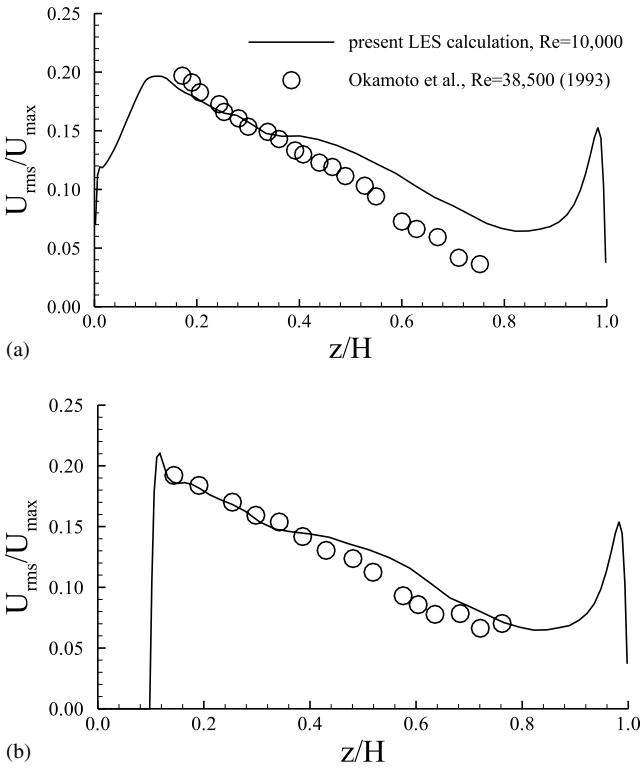

Fig. 13. Comparisons of mean streamwise turbulence intensities with experimental data at cavity and rib for intermediate roughness: (a) at cavity; (b) at rib.

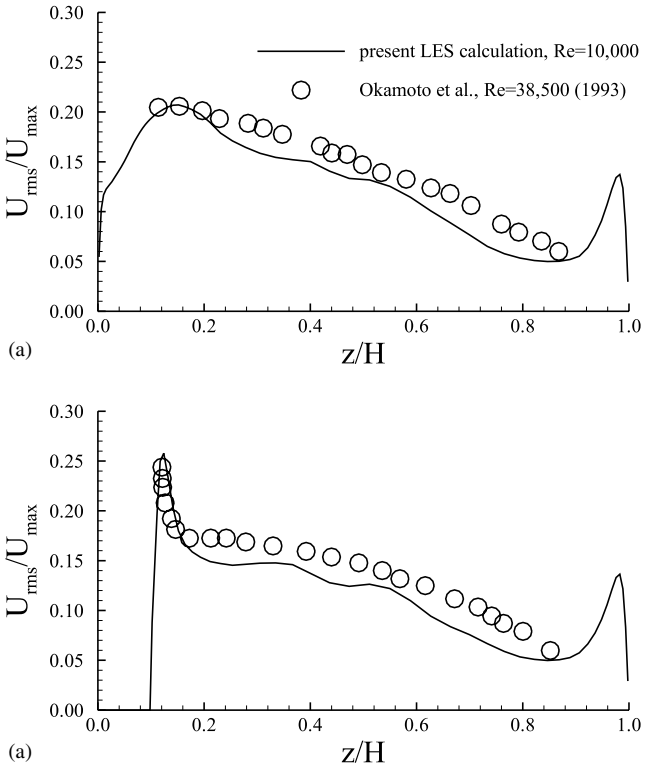

Fig. 14. Comparisons of mean streamwise turbulence intensities with experimental data at cavity and rib for k-type roughness: (a) at cavity; (b) at rib.

boundary layer while the simulations are for channel flow.

Streamwise turbulence intensity is quite large within the cavity for k-type roughness (Fig. 14), indicating penetration of the outer flow deep into the cavity. The ribs intensify the mixing between the flow in the cavities and the outer flow. The highest value of U_{rms} is found at the rib top (Fig. 14(b)), where there is an intense shear layer and local acceleration. The ribs push the minimum U_{rms} between the peaks to $z/H = 0.86$, indicating the effectiveness of k-type roughness in promoting mixing with the outer flow in the channel.

Fig. 15 shows contours of streamwise turbulence intensity U_{rms}. For d-type roughness, U_{rms} in the cavity is negligible. U_{rms} quickly grows to a maximum slightly above the rib height. The contours are almost parallel. For intermediate and k-type roughness, distributions of U_{rms} are similar. Peak values are located at the rib top. This is due to acceleration and strong shear at the rib top. Some local maximum U_{rms} values are found at the top of the main separation zone behind the upstream rib. They are related to the shear layer originating from the rib edge and riding above the separation region. Contours with high U_{rms} are closer to the channel floor, and peaks are higher for k-type than for intermediate roughness.

Fig. 16 shows that the spanwise turbulence intensity, V_{rms}, is enhanced by the ribs. For d-type roughness,

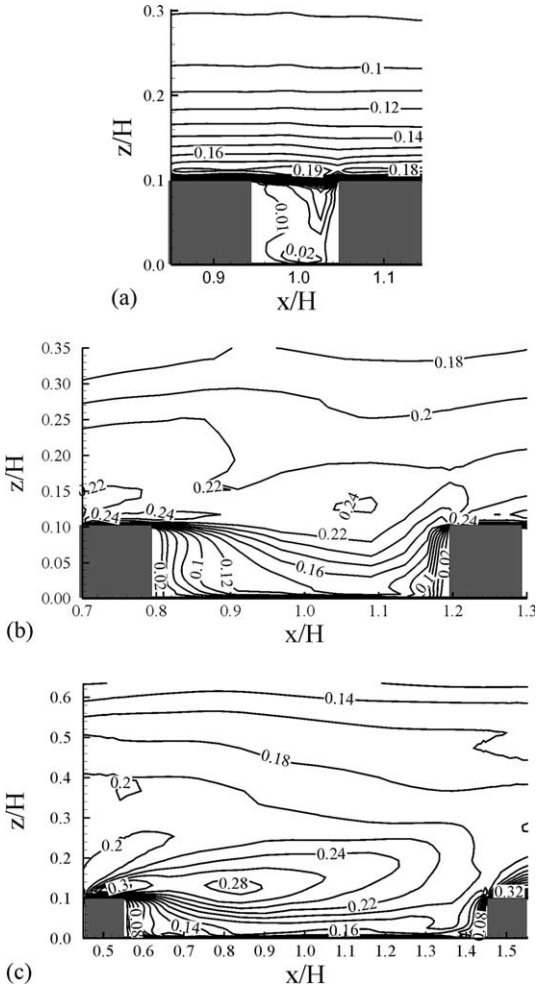

Fig. 15. Mean U_{rms}/U_b contours: (a) d-type roughness; (b) intermediate; (c) k-type roughness.

though V_{rms} magnitude in the cavity is small, compared with outer flow value, it is no longer negligible. For intermediate roughness, the peak value 0.34 lies at the lower corner in front of the rib, where streamwise flow is blocked by the rib. The V_{rms} maximum is even higher than the U_{rms} peak. For k-type roughness, the highest V_{rms} value is also ahead of the rib. High V_{rms} values are also found at the rib top, near the reattachment point in the cavity, and close to the rib front edge.

Vertical velocity fluctuations are displayed in Fig. 17. For d-type roughness, the peak value is at the upper corner in front of the rib. This relates to the flow motion into and out of the cavity. For intermediate and k-type roughness, high W_{rms} values are found in front of the rib, and above the main separation zone inside the cavity. For all three roughness types, W_{rms} is small near the floor in the cavity, indicating weak vertical motions.

Fig. 18 shows contours of the Reynolds shear stress $-\overline{u'w'}$, which is defined as $-\langle(\bar{u} - \langle\bar{u}\rangle)(\bar{w} - \langle\bar{w}\rangle)\rangle/U_b^2$. For d-type roughness there is nearly no contribution to the Reynolds shear stress in the cavity. Right above the

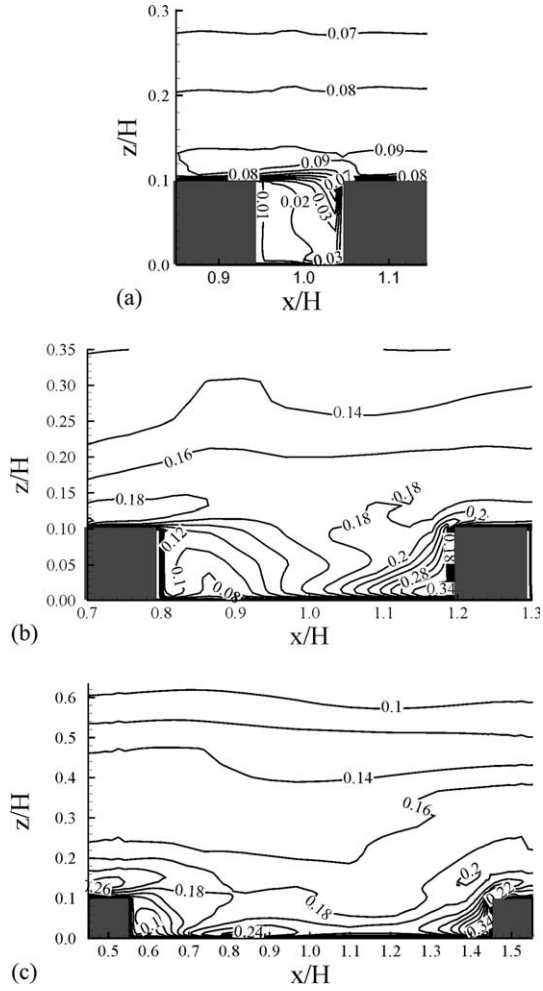

Fig. 16. Mean V_{rms}/U_b contours: (a) d-type roughness; (b) intermediate; (c) k-type roughness.

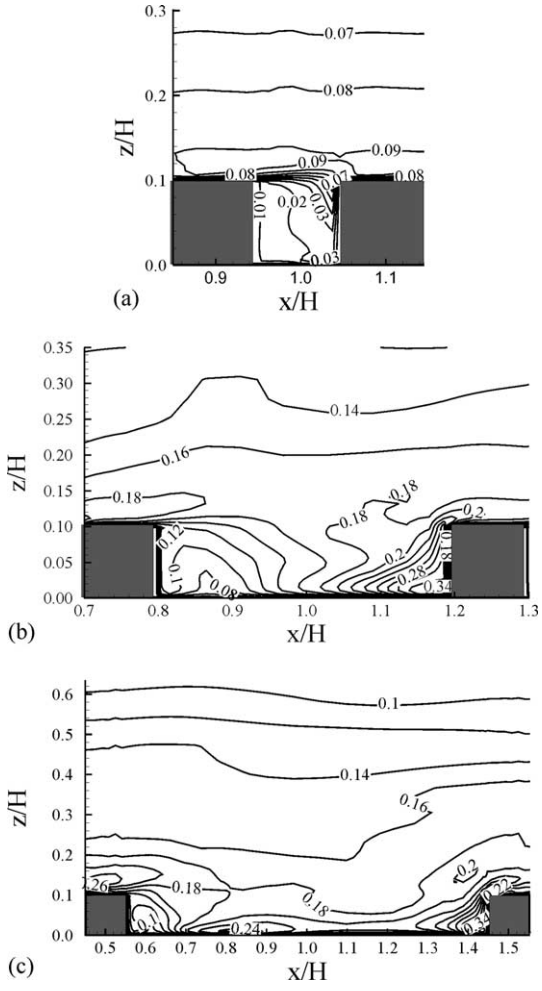

Fig. 17. Mean W_{rms}/U_b contours: (a) d-type roughness; (b) intermediate; (c) k-type roughness.

rib, the shear stress reaches a maximum quickly, then drops slowly to the channel center. The increase in the Reynolds stress near the downstream end of the cavity is consistent with the experimental observation by Djenidi et al. (1999). The peak value of $-\overline{u'w'}$ at the front edge of the rib (Fig. 18(a)) suggests the increase is associated with the inflows and outflows occurring in this region. For intermediate and k-type roughness, the peak $-\overline{u'w'}$ values appear at a downstream distance of about three rib heights and are located above the separation region. Within the recirculation zone behind the rib, the values of $-\overline{u'w'}$ are low.

4. Analysis of ribs as surface roughness

4.1. Resistance components

Resistance to the flow in the channel with rib roughness comprises pressure and friction components. Pressure drag is computed from the pressure difference between the front and back of the ribs. Friction drag on the lower wall includes that from the groove and the rib top. Table 1 summarizes the calculated drag components for a plane channel and the channel with the three types of roughness. The last column in the table shows the pressure force that was imposed to yield a Reynolds number of 10,000 in all cases.

The d-type roughness gives a pressure drag twice that of friction drag. Total drag from the bottom wall (sum of pressure and friction drag) is twice that of the bottom wall in a flat channel (= 0.005, see Table 1). The contribution from the top wall (there is no pressure drag on top wall) is slightly higher than in the flat channel case. The total drag with d-type roughness is considerably higher than for the flat channel. For intermediate and k-type roughness, due to reversed flow in the separation zone behind the rib, the friction drag from the bottom wall is no longer a "drag" force, and is in the direction of the mean flow. The friction drag is negligible compared to the pressure drag. For these two types of roughness, pressure drag is more than 90% of total drag

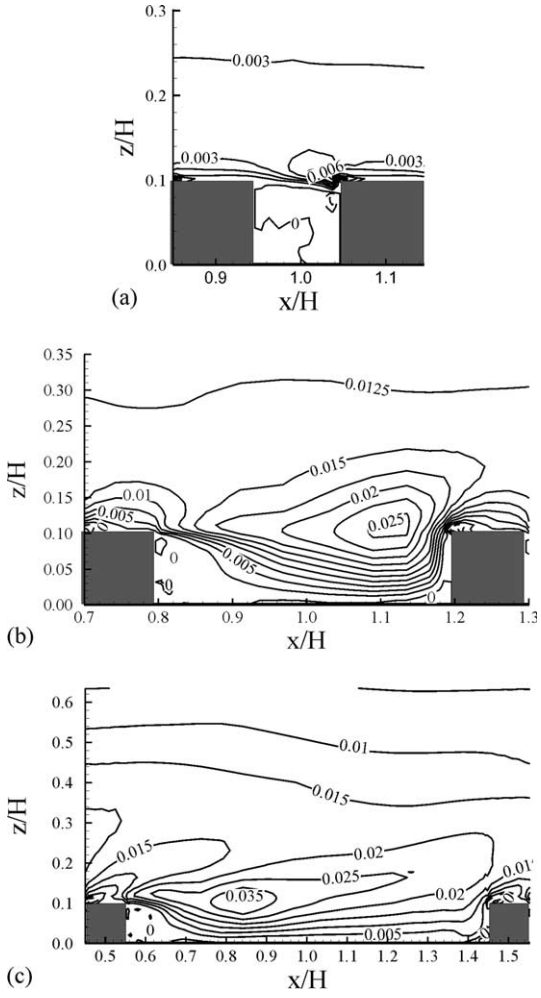

Fig. 18. Mean Reynolds shear stress $-\overline{u'w'}$ contours (normalized by U_b^2): (a) d-type roughness; (b) intermediate; (c) k-type roughness.

of the channel. Most of the remaining drag is attributed to friction on the upper wall. Of the three roughness types, k-type roughness has the highest drag, almost four times that of d-type roughness. As noted above, the last column of Table 1 is the imposed pressure force driving the mean flow. In all cases, the pressure force imposed to drive the mean flow balances total drag from lower and upper surfaces, further validating the numerical method and indicating sufficient sampling times.

4.2. The law of the wall and roughness function

The effect of surface roughness on the mean velocity distribution in a turbulent wall-bounded flow is represented by

$$U/u_\tau = \frac{1}{\kappa}\ln(zu_\tau/\nu) + B - \Delta B \tag{8}$$

where z is measured from a *virtual origin* of the rough wall, u_τ is the *friction velocity*, and ΔB is the *roughness function*. The virtual origin and roughness function depend on the size and type of roughness and both have to be determined by experiment.

The present LES simulations offer an opportunity to determine these quantities for rib roughness. The time and spanwise averaged velocity profiles described in Section 3 were further averaged in the streamwise direction, from one rib center to the next, to obtain the velocity profile to be plotted in the format of Eq. (8). These are shown in Fig. 19. The location where this velocity is zero is defined as the *virtual origin* of the rough surface. For d-type, intermediate, and k-type roughness it is located at $z_0/H = 0.062$, 0.053, and 0.028, respectively, *where z_0 is measured from the bottom of the rib*. The effective *friction velocity* u_τ to be used in Eq. (8) was similarly determined from the *total resistance*, including the pressure and friction components, shown in Table 1. For example, divide the sum of the pressure drag and friction drag (already normalized by $\rho U_b^2 H$) of the lower boundary of the d-type roughness by the surface area to obtain the average stress on the lower surface, then take square root to obtain the friction velocity u_τ. Fig. 20 shows the time and space averaged velocity profiles plotted in law-of-the-wall coordinates. This is perhaps the most surprising result of the LES simulations because in all three cases the velocity profile shows the constant downward shift (same Karman constant, κ) in the logarithmic region, enabling the direct determination of the *roughness function*, ΔB!

Table 2 lists the virtual origin and roughness functions for the three rib configurations. Also included in

Table 1
Resistance components

Flow	Drag force (resistance)				Imposed force
	Lower boundary		Upper boundary	Total	
	Pressure drag	Friction drag			
Plane channel	0.0	0.005	0.005	0.01	0.01
d-Type roughness $w/k = 1$	0.0072	0.0032	0.006	0.0164	0.0164
Intermediate roughness $w/k = 4$	0.0415	−0.0026	0.0067	0.0456	0.0460
k-Type roughness $w/k = 9$	0.0526	−0.0002	0.0074	0.0598	0.0600

Note. Forces are per unit width of channel, and are normalized by $\rho U_b^2 H$.

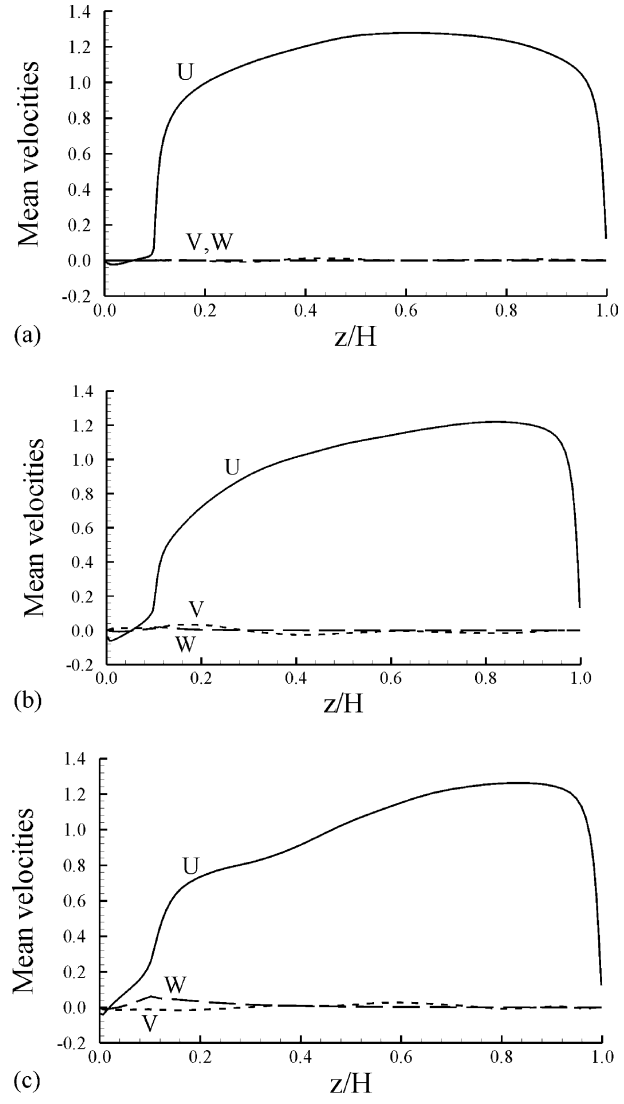

Fig. 19. Averaged mean velocity profiles: (a) d-type roughness; (b) intermediate; (c) k-type roughness.

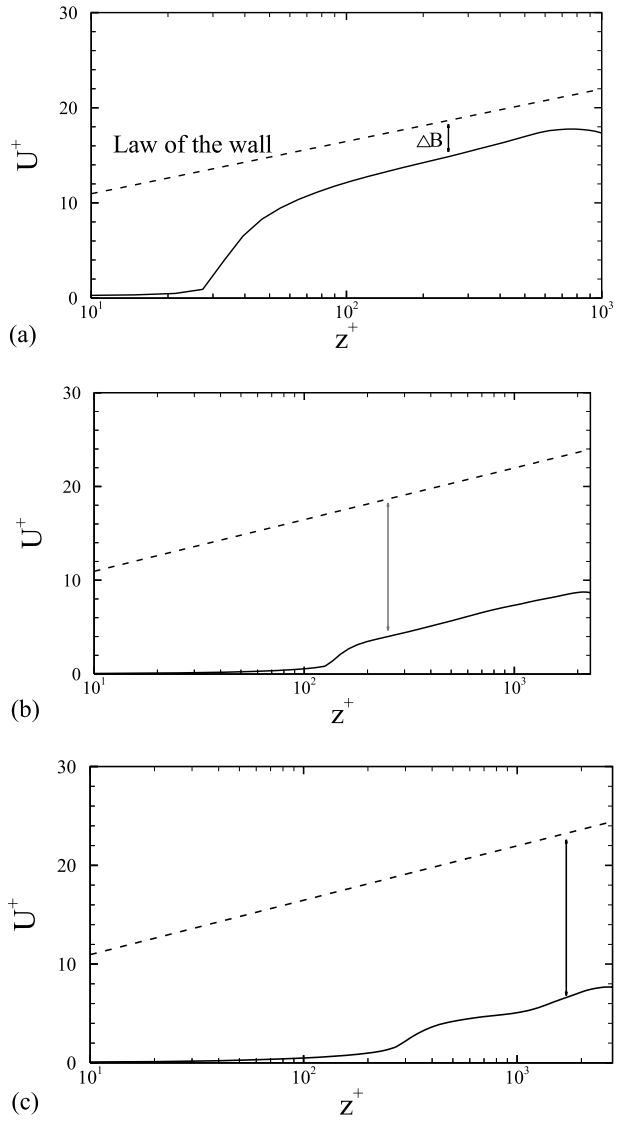

Fig. 20. Averaged streamwise velocity profiles in logarithmic format: (a) d-type roughness; (b) intermediate; (c) k-type roughness.

the table is the *equivalent sand grain roughness*, $k_s^+ = k_s u_\tau / \nu$, determined from the following correlation by Cebeci and Bradshaw (1977) of the famous data of Nikuradse (1950):

$$\Delta B = \left(B - 8.5 + \frac{1}{\kappa} \ln k_s^+ \right) \times \sin[0.4285(\ln k_s^+ - 0.811)] \quad (9)$$

for $2.25 < k_s^+ < 90$, with $B = 5.2$ and $\kappa = 0.42$. For large roughness, $k_s^+ > 90$, this formula reduces to that given in Schlichting (1979).

From Table 2 it is seen that the virtual origin for d-type roughness is closer to the top of the rib than in the other two cases. These trends are consistent with the spatial structure of the flow described earlier (see Fig. 9). The roughness function for k-type roughness is much larger than for d-type roughness. The difference between the roughness function of k-type and intermediate roughness is small. This suggests that there exists an optimum value of the pitch ratio that maximizes the interaction between the roughness layer and the outer flow. Okamoto et al. (1993) found that this optimum ratio was 9 in their experiment, as it gave maximum turbulence and heat transfer augmentation, and hence the highest heat transfer coefficient. The present LES results tend to confirm this experimental observation.

The equivalent sand grain roughness for the three rib configurations shows that intermediate and k-type roughness are much more effective in generating resistance than sand grain roughness. For example, sand grains of height $5.9k$ ($0.59H$) along the entire lower wall of the channel would be needed to produce the resistance generated by only two ribs of height k! This result shows just how crude is the concept of equivalent sand grain roughness.

Table 2
Virtual origins and roughness functions

Roughness	z_0/H	z_0/k	z_0^+	ΔB	k_s^+	k_s/k
d-Type	0.062	0.62	89.3	3.6	16.1	0.1
Intermediate	0.053	0.53	147.8	13.2	891	3.2
k-Type	0.028	0.28	90.6	15.0	1891	5.9

Note. z_0 is measured from the bottom of the ribs.

5. Instantaneous velocity field

Fig. 21 shows instantaneous velocity vectors in six (x, y) planes for k-type roughness. At $z/H = 0.02$ from the bottom surface (Fig. 21(a)), random turbulent motions caused by the ribs are observed over the entire plane. Many downstream and upstream traveling eddies imply the presence of multiple separation regions. Spanwise motions occur frequently, especially in front of the ribs. Fig. 21(b) is at $z/H = 0.09$, directly below the rib top, and Fig. 21(c) is at $z/H = 0.12$, directly above. These two plots show the rapid change of flow field caused by the ribs near the rib top. They appear to be correlated. Above the rib, higher velocities are populated with few spanwise motions. The existence of upstream motions indicates the presence of separation zones beyond the cavity between the ribs, but they are weak. Away from the rib top the reversed flow vanishes at $z/H = 0.25$ (Fig. 21(d)). However, the flow field still shows correlation to the two ribs. Stronger motions are concentrated above the ribs. At the channel center (Fig. 21(e)), the vector plot displays little correlation with the ribs and the velocity field is dominated by the streamwise flow. Close to the top wall (Fig. 21(f)), the flow is quite smooth and without any reversal of direction. Some streaky structures exist, similar to those in flat channel flow.

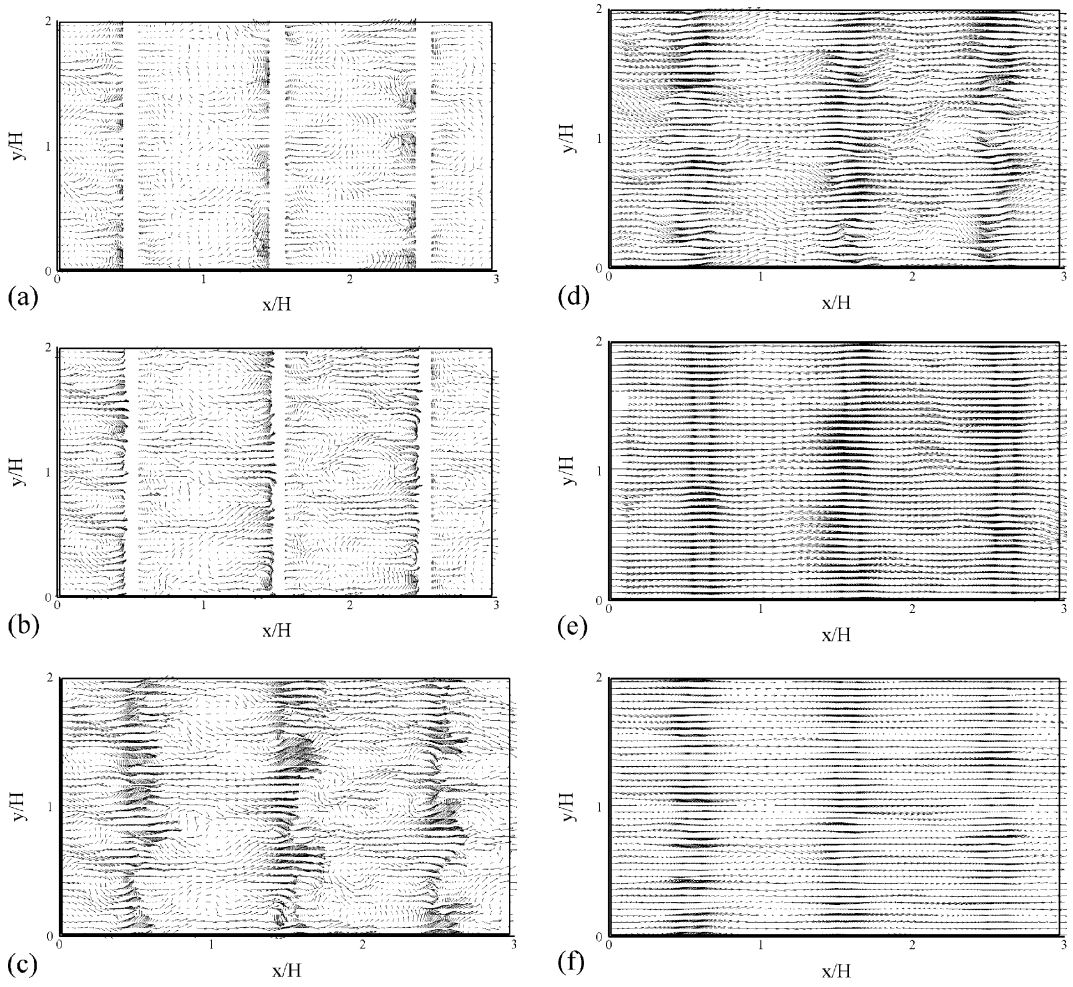

Fig. 21. Instantaneous velocity vectors in six (x, y) planes at $z/H = 0.02$ (a), 0.09 (b), 0.12 (c), 0.25 (d), 0.50 (e), 0.9 (f), for k-type roughness.

The instantaneous velocity vectors at three spanwise locations are plotted in Fig. 22. Velocity overshoot above the rib top is confirmed in these figures, e.g., Fig. 22(a). The strong favorable pressure gradient accelerates flow on the rib top. Multiple separation regions are formed in front of and behind the ribs, with their size and shape varying greatly in spanwise and streamwise directions. Some of these separation regions are found well beyond the cavity between the ribs. Circulation generated by these separation zones brings faster fluid into the cavity and takes slower fluid into the outer flow. Interaction between flow within the roughness layer and the outer flow is significantly intensified by rib roughness.

Instantaneous velocity vectors at six streamwise locations are shown in Fig. 23. At the rib top (Fig. 23(a)), strong vortical structures are found directly above the rib. Slightly downstream of the rib (Fig. 23(b)) there is an "interface" at rib height. Above this interface, vortical structures from the upstream rib top persist at about the same height. Below the interface, some spanwise motions begin to appear. At $x/k = 1.9$ (Fig. 23(c)), the interface disappears due to flow mixing across it. Strong vortical structures are located close to the cavity floor. At $x/k = 4.2$ (Fig. 23(d)) and $x/k = 6.6$ (Fig. 23(e)), close to the mean reattachment and detachment points (refer to Fig. 5(c)), respectively, downward and upward flows are expected. However, these two snapshots do not show the dominance of such motions. This suggests that reattachment and detachment points vary significantly in location, and can be determined only statistically. Fig. 23(f) is at $x/k = 8.8$, immediately in front of the downstream rib. The near-wall flow is dominated by strong spanwise motion due to the rib blockage effect.

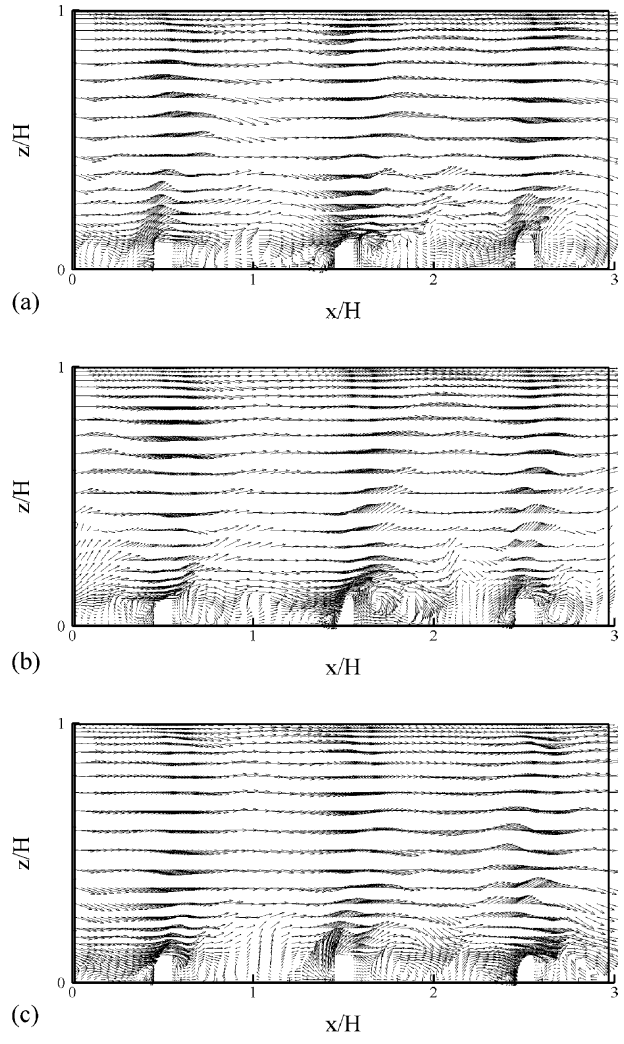

Fig. 22. Instantaneous velocity vectors in three (x,z) planes at $y/H = 0.5$ (a), 1.0 (b), 1.5 (b), for k-type roughness.

Similar analysis of d-type roughness does not provide more insight into the turbulent structures associated with the ribs because the interaction between the flows inside and outside of the roughness layer is quite weak even in the instantaneous plots compared with the other two roughness types. The characteristics of the instantaneous flow field of intermediate roughness are similar to those of k-type roughness with some variations in intensity.

6. Conclusions

The present LES calculations agree with the rib roughness classifications that were made on the basis of laboratory experiments. Based on pitch ratio, rib roughness is divided into d-type and k-type. Closely spaced ribs result in d-type roughness. The cavity between the ribs is filled, in a time-average sense, by a relatively weak eddy that does not interact with the flow outside the roughness layer. The limit of d-type roughness appears to be a pitch ratio of 4, when the eddy just fills the gap between the ribs, and reattachment occurs at the top front of the downstream rib. We have used the term intermediate roughness to describe this case. A k-type roughness is associated with pitch ratios greater than 4. Then the main eddy in the groove between the ribs is about 4 rib heights long, and there are several smaller eddies. This type of roughness leads to strong interaction between the flow in the roughness layer and the outer flow.

The LES simulation shows that surface roughness elements in the form of ribs impose their own characteristic length scales (rib height and cavity length) on near-wall flow structures. In addition to general length and time scales for channel flow, length and time scales related to roughness elements must be taken into account to properly describe the flow close to and within the roughness layer.

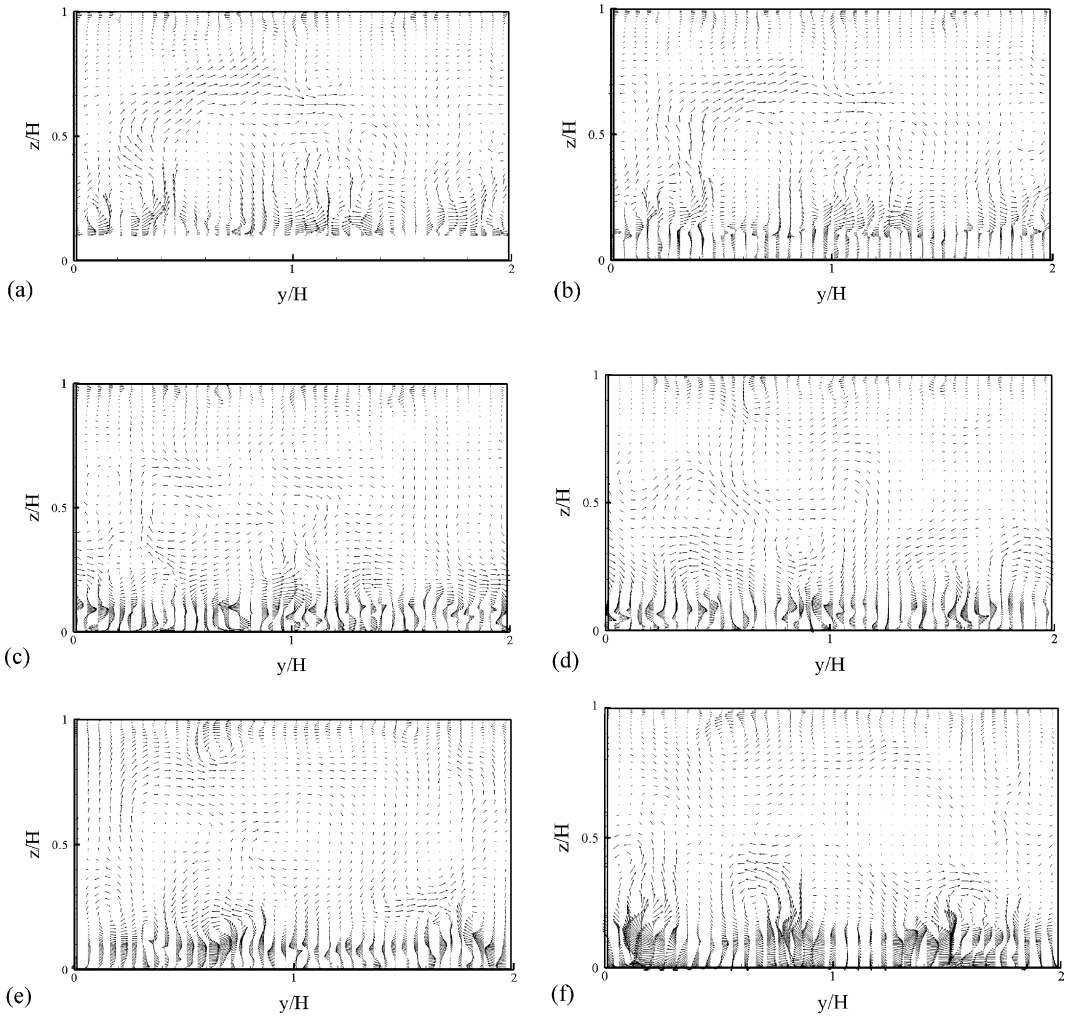

Fig. 23. Instantaneous velocity vectors in six (y,z) planes at $x/k = -0.5$ (a; the rib top), 0.2 (b), 1.9 (c), 4.2 (d), 6.6 (e), 8.8 (f), for k-type roughness (the distance x is measured from the back face of the upstream rib).

It is shown that LES can be used to identify the pressure and frictional components of resistance in a rib-roughened channel. A particularly noteworthy result is that time and space averaging of the grossly three-dimensional, unsteady and spatially varying structure of this complex flow leads to the classical semi-logarithmic velocity distribution, displaced from the law of the wall for smooth walls by the so-called roughness function. In fact, the roughness function and location of the associated virtual origin of the rough wall can be determined by LES. This creates the interesting possibility of using LES to explore parametric variations in rib roughness, and indeed other types of roughness, and determining, for the first time, the connection between roughness geometry and its gross effect on the outer flow as manifested in the simplified concepts of roughness functions and equivalent sand grain roughness.

It is commonly believed that for d-type roughness, the roughness function is related to the pipe diameter d (or channel height H, or boundary layer thickness δ), and this is the reason why it is named d-type. The present LES calculation and experiment by Djenidi et al. (1999) suggest that the flow structures near the roughness elements also depend on the rib height k. For intermediate and k-type roughness, strong dependency on roughness height k is apparent. However, flow far away from the roughness element is also affected. This is consistent with the experimental measurements of rough-wall turbulent boundary layer by Krogstad et al. (1992). The fact that roughness effects extend into most of the flow has significant implications for RANS type modeling. The observation that the ribs on the bottom wall influence the resistance on the top wall of the channel suggests a large scale interaction between the flow in the roughness layer and the outer flow. In turn, this indicates that the flow over roughness involves more scales than just d or k, and the conventional naming of the roughness type is an over simplification. A more

systematic and comprehensive classification of flow over rough surfaces needs to be developed, and LES can be of great value in such studies.

Acknowledgements

The authors acknowledge the computer facilities and services provided by IIHR—Hydroscience and Engineering (formerly Iowa Institute of Hydraulic Research), National Center for Supercomputing Applications, and National Partnership for Advanced Computational Infrastructure. Professor Robert Street and Dr. Yan Zang made available the source code developed at Stanford University.

References

Antonia, R., Luxton, R.E., 1971. The response of a turbulent boundary to an upstanding step change in surface roughness. ASME J. Basic Eng. 93, 22–34.

Bredberg, J., Davidson, L., 1999. Prediction of flow and heat transfer in a stationary two-dimensional rib roughened passage using low-*Re* turbulent models. In: Third European Conference on Turbomachinery, IMech C557/074/99, pp. 963–972.

Cebeci, T., Bradshaw, P., 1977. Momentum Transfer in Boundary Layers. Hemisphere Publishing Corporation.

Ciofalo, M., Collins, M.W., 1992. Large-eddy simulation of turbulent flow and heat transfer in plane and rib-roughened channels. Int. J. Numer. Methods Fluids 15, 453–489.

Djenidi, L., Elavarasan, R., Antonia, R.A., 1999. The turbulent boundary layer over transverse square cavities. J. Fluid Mech. 395, 271–294.

Durst, F., Founti, M., Obi, S., 1988. Experimental and computational investigation of the two-dimensional channel flow over two fences in tandem. J. Fluids Eng. 110, 48–54.

Germano, M., Piomelli, U., Moin, P., Cabot, W.H., 1991. A dynamic subgrid-scale eddy viscosity model. Phys. Fluids A 3, 1760–1765.

Hanjalic, K., Launder, B.E., 1972. Fully developed asymmetric flow in a plane channel. J. Fluid Mech. 51, 301–335.

Hussain, A.K.M.F., Reynolds, W.C., 1975. Measurements in fully developed turbulent channel flow. J. Fluids Eng. 97, 568–578.

Islam, O., Logan, E., 1976. Channel flow over smooth-to-rough surface discontinuity with zero pressure gradient. J. Fluids Eng. 99, 626–634.

Krogstad, P.A., Antonia, R.A., Browne, L.W., 1992. Comparison between rough- and smooth-wall turbulent boundary layers. J. Fluid Mech. 245, 599–617.

Lilly, D.K., 1992. A proposed modification of the Germano subgrid-scale closure method. Phys. Fluids 4, 633–635.

Liou, T.M., Chang, Y., Hwang, D.W., 1990. Experimental and computational study of turbulent flows in a channel with two pairs of turbulent promoters in tandem. J. Fluids Eng. 112, 302–310.

Liou, T.M., Hwang, J.-J., Chen, S.-H., 1993a. Simulation and measurement of enhances turbulent heat transfer in a channel with periodic ribs on one principal wall. Int. J. Heat Mass Transfer 36, 507–517.

Liou, T.M., Wu, Y.Y., Chang, Y., 1993b. LDV measurements of periodic fully developed main and secondary flows in a channel with rib-distributed walls. J. Fluids Eng. 115, 109–114.

Miyake, Y., Tsujimoto, K., Nakaji, M., 2001. Direct numerical simulation of rough-wall heat transfer in a turbulent channel flow. Int. J. Heat Fluid Flow 22, 237–244.

Moser, R.D., Kim, J., Mansour, N.N., 1999. Direct numerical simulation of turbulent channel flow up to $Re_\tau = 590$. Phys. Fluids 11, 943–945.

Najjar, F.M., Tafti, D.K., 1996. Study of discrete test filters and finite difference approximations for the dynamic subgrid-scale stress model. Phys. Fluids 8, 1076–1088.

Nikuradse, J., 1950. Laws of flow in rough pipes. National Advisory Committee for Aeronautics, NACA TM 1292 (Translation from VDI-Forschungsheft 361, 1933).

Okamoto, S., Seo, S., Nakaso, K., Kawai, I., 1993. Turbulent shear flow and heat transfer over the repeated two-dimensional square ribs on ground plane. J. Fluids Eng. 115, 631–637.

Patel, V.C., 1998. Perspective: flow at high Reynolds number and over rough surfaces—Achilles Heel of CFD. J. Fluids Eng. 120, 434–444.

Perry, A.E., Schofield, W.H., Joubert, P.N., 1969. Rough wall turbulent boundary layers. J. Fluid Mech. 37, 383–413.

Piomelli, U., 1993. High Reynolds number calculations using the dynamic subgrid-scale stress model. Phys. Fluids 5, 1484–1490.

Schlichting, H., 1979. Boundary-Layer Theory, seventh ed. Series in Mechanical Engineering, McGraw-Hill, New York.

Siuru, W.D., Logan Jr., E., 1977. Response of a turbulent pipe flow to a change in roughness. J. Fluids Eng. 99, 548–555.

Tani, J., 1987. Turbulent boundary layer development over rough surfaces. In: Perspectives in Turbulence Studies. Springer.

Wei, T., Willmarth, W.W., 1989. Reynolds-number effects on the structure of a turbulent channel flow. J. Fluid Mech. 204, 57–95.

White, F.M., 1991. Viscous fluid flow, second ed. McGraw-Hill, New York.

Zang, Y., Street, R.L., Koseff, J.R., 1994. A non-staggered grid, fractional step method for time-dependent incompressible Navier–Stokes Equations in curvilinear coordinates. J. Comp. Phys. 114, 18–33.